Aerodynamic Performance of a Topologically Optimised Nose-Wheel Fork of a Light Aircraft Produced By Selective Laser Melting

L.F. Monaheng[1*], W.B. du Preez[2] & C. Polese[3,4]

ARTICLE INFO

Article details
Presented at the 26th annual conference of the Rapid Product Development Association of South Africa, held from 27 to 30 October 2025 in Pretoria, South Africa

Available online 8 Dec 2025

Contact details
* Corresponding author
lmonaheng@cut.ac.za

Author affiliations
1 Department of Mechanical and Mechatronics Engineering, Faculty of Engineering, Central University of Technology, Free State, South Africa

2 Centre for Rapid Prototyping and Manufacturing, Central University of Technology, Free State, South Africa

3 School of Mechanical, Industrial and Aeronautical Engineering, University of the Witwatersrand, South Africa

4 ARUA Centre of Excellence in Materials, University of the Witwatersrand, South Africa

ORCID® identifiers
L.F. Monaheng
https://orcid.org/0000-0002-2263-3162

W.B. du Preez
https://orcid.org/0000-0001-9935-7330

C. Polese
https://orcid.org/0000-0003-2662-8114

DOI
http://dx.doi.org//10.7166/36-3-3346

ABSTRACT

A complex topologically optimised landing gear fork for a light aircraft was fabricated using selective laser melting (SLM). It was hypothesised that the optimised fork would exhibit a unique air flow surface contour that could enhance aerodynamic performance by promoting lift and reducing drag compared with conventionally manufactured components. To test this hypothesis, the aerodynamic behaviour of the nose-wheel fork was investigated using computational fluid dynamics (CFD). Both the SLM-produced optimised fork and a conventionally milled counterpart were analysed to predict lift and drag. The findings provide insight into the potential of topology optimisation to improve the aerodynamic efficiency of aircraft structures.

OPSOMMING

'n Komplekse topologies optimeerde landingsonderstelvurk vir 'n ligte vliegtuig is vervaardig met behulp van selektiewe lasersmelting (SLM). Daar is gehipotetiseer dat die optimeerde vurk 'n unieke lugvloei-oppervlakkontoer sou vertoon wat aërodinamiese prestasie kan verbeter deur draagkrag te bevorder en lugweerstand te verminder in vergelyking met konvensioneel vervaardigde komponente. Om hierdie hipotese te toets, is die aërodinamiese gedrag van die neuswielvurk ondersoek met behulp van berekeningsvloeidinamika (CFD). Beide die SLM-vervaardigde geoptimaliseerde vurk en 'n konvensioneel gefreesde eweknie is geanaliseer om draagkrag en lugweerstand te voorspel. Die bevindinge bied insig in die potensiaal van topologie-optimalisering om die aërodinamiese doeltreffendheid van vliegtuigstrukture te verbeter.

1. INTRODUCTION

Metal additive manufacturing (AM) has the potential to build fully functional structural components of aircraft [1]. The goal of applying AM is to reduce production time and the wastage of raw material. Parts are built layer by layer as powder is deposited and selectively fused into previously solidified layers, thereby forming three-dimensional (3D) components. Selective laser melting (SLM) was chosen for its ability to produce highly intricate geometries with superior precision, compared with direct metal deposition (DMD) and electron beam melting (EBM) [2].

A titanium alloy that is often used to produce aircraft parts through SLM is Ti6Al4V(ELI) [3][4]. This alloy is applied because of its excellent corrosion resistance, high strength, and low density [5]. Moreover, the outstanding fatigue resistance of Ti6Al4V(ELI) makes it appealing for the production of mission-critical parts, such as landing gear, offering clear advantages over conventional metals such as aluminium alloys [6].

The landing gear is a subsystem of an aircraft that is essential for landing, taxiing, and take-off, and it must be designed in compliance with the required safety regulations [7]. Designing landing gear without due consideration of its aerodynamic effect has a negative impact on its performance, since it causes a significant amount of parasite drag and unwanted weight on the aircraft [8]. The large structural components of a landing gear, such as the nose-wheel fork, should be designed to generate aerodynamic low pressure on the upper surface and high pressure on the lower surface. According to Bernoulli's principle, this pressure differential is achieved by increasing airflow velocity over the upper surface and reducing it over the lower surface, thereby promoting lift [9].

The integration of topology optimisation into the design for additive manufacturing (DfAM) results in complex-shaped components that are difficult, if not impossible, to produce with traditional milling technology, but that are quite feasible with AM [9]. This optimisation technology offers more than 20% mass saving without compromising the required strength [10]. It was hypothesised that topology optimisation could result in aerodynamically sound geometrical shapes. The most widely used topology optimisation algorithm is the solid isotropic material with penalisation (SIMP), which is preferred over sequential linear programming (SLP) and sequential quadratic programming (SQP) because of its compatibility with finite element analysis platforms [11]. In topology optimisation, the objective function is typically to minimise compliance – for example, redistributing material within a prescribed design domain so as to generate layouts that maximise the geometric stiffness of the resulting structural components [12]. This results in organic-shaped components that are characterised by irregular, natural shapes. As a result, the optimised structures can also conform to aircraft airfoil-shaped structural components that promote lift and reduce drag [13].

Nonetheless, the new design of a structural part of an aircraft must be certified for its application before acceptance [7]. Certification by analysis (CbA) could be applied to reduce the physical experimental testing, which is often expensive and time-consuming [14]. Computational fluid dynamics (CFD) is one of the methods used to predict the aerodynamic performance of aircraft components [15]. It has been found to be an effective tool for understanding flow phenomena in various parts of the aviation industry [15]. During CFD simulation of aerodynamic forces and the flow field around a complex-shaped part of an aircraft, finite volume discretisation with Reynolds-averaged Navier-Stokes (RANS) is commonly applied to model turbulent airflow [16]. RANS has gained popularity because of its ability to generate accurate results at a moderate computational cost. Other airflow modelling, such as the large eddy simulation (LES), is ten times more computationally demanding than RANS [17].

A detailed, experimentally validated CFD simulation of retractable landing gear loads has been published in a previous study [18]. Imamura *et al.* [19] analysed the aerodynamics and aero-acoustics of a two-wheel landing gear. Spalart *et al.* [18] tested the rudimentary features of the landing gear and predicted their performance using the CFD technique. However, the effect of topology optimisation on the aerodynamic performance of landing gear remains unexplored.

In the current study, the aerodynamic performance of the topologically optimised computer-aided design (CAD) model nose-wheel fork of an advanced high-performance reconnaissance light aircraft (AHRLAC) that was redesigned for building in Ti6Al4V(ELI) through SLM was investigated. For this, CFD with RANS turbulence modelling was applied to understand the wall shear stress, the velocity and pressure distribution, and the lift and drag force experienced by the fork. To demonstrate the benefits of topology

optimisation, CFD analysis was also carried out on the original nose-wheel fork manufactured from aluminium alloy 7050 using conventional milling, and the results were compared with those of the topology-optimised one. The comparison covered the velocity, pressure distribution, shear wall stress, and drag and lift forces of the optimal and the original nose-wheel fork. It is shown here that topology optimisation resulted in a significant improvement of the aerodynamic performance of the AHRLAC nose-wheel fork.

2. THEORETICAL FRAMEWORK

Topology optimisation through the SIMP algorithm seeks an optimal design (Ω_{mat}), which is contained in the available design domain ($\boldsymbol{\Omega}$) [20]. The available design domain is partitioned into void and solid elements by finite element discretisation. In this case, the design variable is represented by the density vector containing elemental density (ρ_e). Consequently, the local stiffness tensor ($E(\rho_e)$) is formulated by incorporating the density vector and the component of stiffness (E_0), as shown in Equation 1:

$$E(\rho_e) = \rho_e^p E_0 \tag{1}$$

The elemental density in the design variable is applied using Equation 2 [9], where the elastic modulus of the elements (e) is reduced to element stiffness (K_e). Consequently, the SIMP stiffness can be expressed as in Equation 3.

$$\rho_e = \begin{cases} 0 & if\ e \in \Omega/\Omega_{mat} \\ 1 & if\ e \in \Omega_{mat} \end{cases} \tag{2}$$

$$K_{SIMP(\rho)} = \sum_{e=1}^{N} \left[\rho_{min} + (1-\rho_{min})\rho_e^p\right] K_e \tag{3}$$

where p is the penalising factor that penalises elements with intermediate density to approach 0 (void) or 1 (solid element), and ρ_{min} represents the lower density value limit to avoid singularities. Finally, optimisation results in a structural component that has the potential to improve aerodynamic performance, as illustrated in Figure 1.

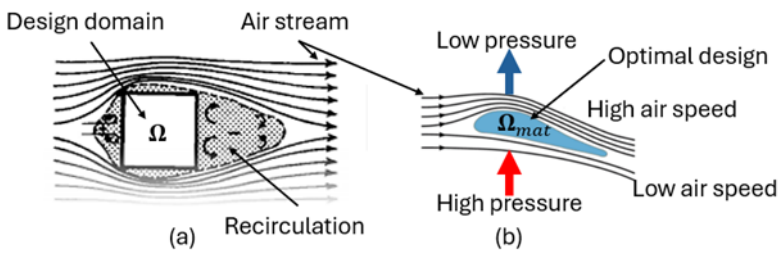

Figure 1: An illustration of the theory that topology optimisation could improve the aerodynamic performance of structural components of aircraft, (a) design domain and (b) optimal design.

When defining the airflow following Bernoulli's Equation 4, the optimal design would have better lift than the design domain owing to the variation of airflow speed between the upper and lower surfaces. Moreover, reduced drag force will be experienced by the optimal design, since there is no recirculation.

$$P + \frac{\rho_{V^2}}{2} + \rho g h = \text{constant} \tag{4}$$

where P, ρ, V, g and h represent static pressure, fluid density, air velocity, gravitational acceleration and height, respectively. To predict the aerodynamic performance, the RANS formulation in Equation 5 is solved in the CFD modelling for a given dynamic viscosity (μ) of the flow [21].

$$\rho \frac{\partial \overline{\rho u_i}}{\partial t} + \frac{\partial}{\partial x_j}(\overline{\rho u_i}\,\overline{u}_j) = -\frac{\partial \overline{p}}{\partial x_i} + \mu \frac{\partial^2 \overline{u_i}}{\partial x_j \partial x_j} - \frac{\partial}{\partial x_j}(\overline{\rho u_i' u_j'}) \tag{5}$$

where t is time, and u_i, and u_j are the velocity components in i and j directions, respectively. The u_i' and u_j' represent the fluctuating velocity components, also in i and j directions. Finally, x_i and x_j stand for the

coordinates in the *i* and *j* directions. The solution of Equation 5 allows the prediction of turbulent modelling that results in a significant fluctuation of flow properties. These include the velocity and pressure distribution as well as the shear stress.

3. MATERIAL AND METHODS

The nose-wheel fork of the AHRLAC was redesigned by using the topology optimisation software Altair SolidThinking Inspire® [22], and the design was structurally verified by MSC Nastran/Patran® software [23]. The objective was to obtain a balanced strength-to-weight ratio from the original CAD model of the AHRLAC fork that was produced through a conventional milling process. The detailed design procedure is described in [24], whereas the production in Ti6Al4V(ELI) through SLM and the mechanical performance of this topologically optimised nose-wheel fork were published by Monaheng *et al.* [25]. The original and topologically optimised CAD models of the AHRLAC nose-wheel fork are shown in Figures 2(a) and (b), respectively.

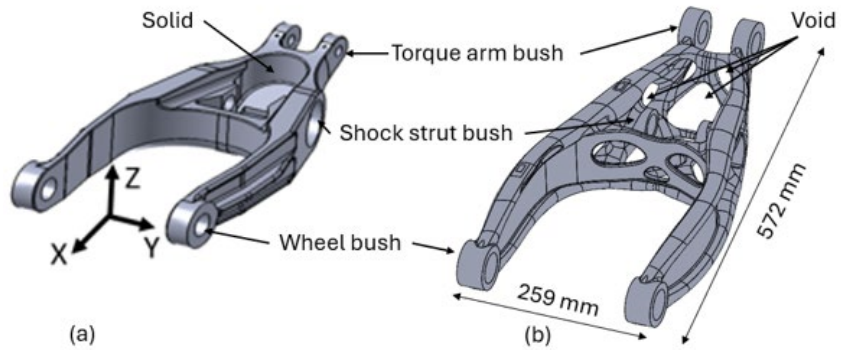

Figure 2: CAD model of nose-wheel fork, (a) original fork and (b) topologically optimised fork.

To predict the aerodynamic behaviour of the full-scale nose-wheel fork, the scFlow V2020 CFD software [26] was used for both the original CAD model and the CAD model of the optimised fork. For this simulation, a virtual wind tunnel was created, as shown in Figure 3(a). The angle of attack between the torque arm and shock strut bush was 37.81°, whereas that between the shock strut and wheel bush was 18.36°, to reproduce the conditions during the aircraft's take-off; in the model, the incompressible air was set with an inlet take-off speed of 28 m/s, assuming that the air stream impinging on the surface of the fixed nose-wheel fork in the wind tunnel was equivalent to the fork of an aircraft moving through the air when the aircraft become airborne. Moreover, the air and the fork were discretised using polyhedral elements, as illustrated in Figure 3(b). The Z- and X-axis were along the lift and drag directions, respectively, whereas the Y-axis was pointing towards the side wall.

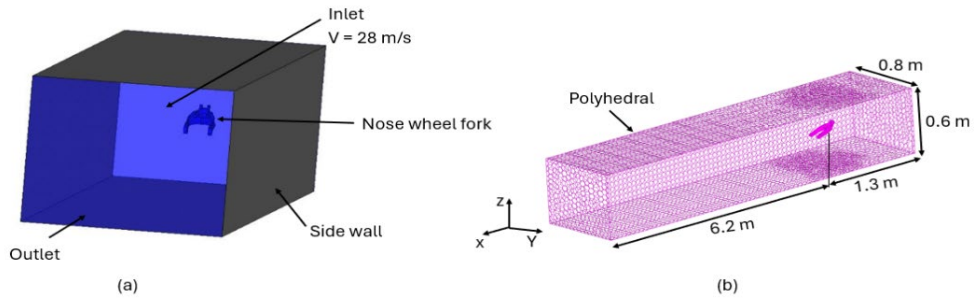

Figure 3: (a) Virtual wind tunnel with nose-wheel fork, and (b) discretisation of incompressible air and the nose-wheel fork.

For the surface of the fork and the air around it, a mesh size of 1.563 mm was generated to obtain accurate results. On the other hand, in regions of the air that were far from the fork, a mesh size of 12.5 mm was generated to reduce computational time. In Table 1, the thermal and material properties of the

incompressible air and of the original and optimised nose-wheel forks that were used during the simulation are listed.

Table 1: Thermal and material properties of the incompressible air and the original and optimised nose-wheel forks

Nose-wheel fork	Materials	Density (kg/m^3)	Specific heat J/(kg·K)	Thermal conductivity W/(m·K)	Thermal expansion (1/K)	Viscosity (Pa·s)
-	Incompressible air	1.206	-	0.0256	0.003411	18.3e-6
Original	AA7050	2700	860	157	-	-
Optimised	Ti6Al4V(ELI)	4420	537	7.6	-	-

A steady-state analysis incorporating gravitational effects was carried out, as the density of the original nose-wheel fork differed from that of the optimised design. Since this study aimed to investigate the influence of topology optimisation on aerodynamic performance, a steady-state simulation was deemed most appropriate. To validate this condition, airflow velocity and temperature during take-off were kept constant. The constant temperature also ensured that thermal effects were excluded from the results.

Moreover, it was assumed that both forks exhibited the same surface roughness. The simulations were conducted using a turbulence fluid flow model (RANS with sensitivity of shear stress transport (SST) k-ω), as RANS is widely recognised for predicting aerodynamic performance in engineering applications [27]. Finally, the fork was virtually sectioned in the ZX and XY planes to help the interpretation of the CFD results, which were driven by the design geometry and the material properties of the original and the optimised nose-wheel forks.

4. RESULTS AND DISCUSSION

The aerodynamic performance of the original and the optimised nose-wheel forks is presented in this section. The characteristics that were examined were velocity, pressure distribution, wall shear stress, and drag and lift forces. By presenting these results, a performance comparison between the original and optimised forks can be discussed, highlighting the effects of design shape and material properties on their aerodynamic behaviour.

4.1. Velocity distribution

In Figure 3(a)–(b) and (c)–(d), the velocity vectors of the air stream passing along the ZX plane and the XY plane, respectively, of the original and topologically optimised nose-wheel forks are shown. In the original and the optimised nose-wheel forks, the velocity vectors demonstrated different air streams on the surface of the fork. This was attributed to the various surface contours of the two forks. The resistance of airflow on the original fork is indicated by the direction of the velocity vectors, which oppose the airflow stream. This contributes to the drag force on the original nose-wheel fork, which translates to higher fuel consumption by the aircraft [28]. An airflow recirculation from the surface of the original nose-wheel fork was also observed. Moreover, a maximum and minimum airflow velocity were found on the lower and upper surfaces, respectively, of the original fork. Unlike the original fork, the optimised one had a void in the front area, allowing a smooth air flow, and no recirculation was identified in the region shown in Figure 4. The upper and lower surfaces experienced minimal and maximum air flow speed at levels higher than those recorded on the original nose-wheel fork.

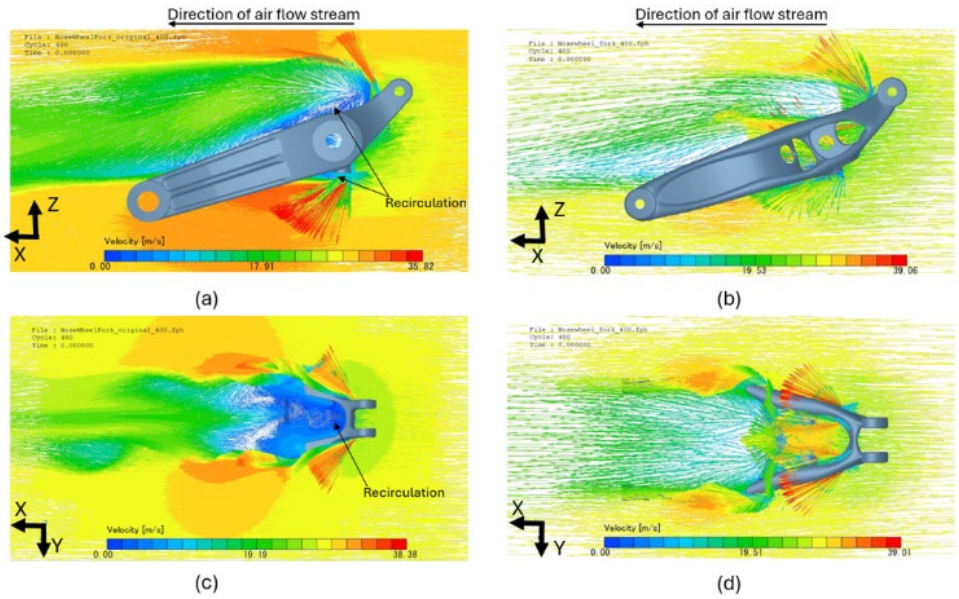

Figure 4: The velocity vectors of the air stream passing along the ZX ((a) and (b)) and XY planes ((c) and (d)) of the nose-wheel fork. Images (a) and (c) show the original fork, whereas (b) and (d) are of the topologically optimised fork.

4.2. Pressure distribution

The pressure distribution on the surfaces of the original and optimised nose-wheel forks is shown in Figure 5. This illustrates the pressure difference resulting from the topologically optimised geometry of the fork.

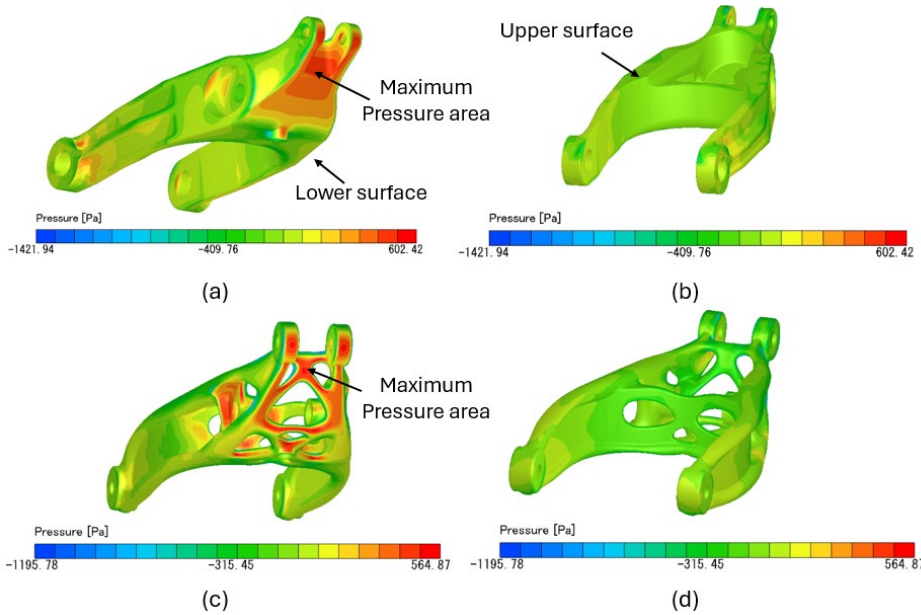

Figure 5: The relative pressure distribution on the surfaces of the nose-wheel fork; (a) and (b) show the original fork, whereas (c) and (d) show the optimised fork.

In both the original and the optimised nose-wheel forks, there is a pressure difference between the upper and lower surfaces. Higher pressure was observed on the lower surface of the nose-wheel fork, while lower pressure was detected on the upper surface. The pressure difference of 38.07% and 56.67% between the upper and lower surfaces of the original and optimised forks, respectively, suggested that the topology-optimised fork would promote lift better than the original fork. This higher percentage pressure difference of the optimised nose-wheel fork was attributed to the high speed of airflow observed on the upper surface. It followed Bernoulli's equation, which specifies that increasing speed results in a decrease in pressure and vice versa [29]. Moreover, the pressure is at a maximum on the lower surface where the angle of attack is higher. This behaviour was observed for both the original and the optimised nose-wheel forks, and it is a well-known phenomenon in flight aerodynamic studies [30].

Figures 6(a) and (c) show the detailed views of the respective pressure distribution in the mid-section (plane ZX) of the original and the optimised nose-wheel forks. In addition, Figures 6(b) and (d) are graphical representations of the magnitudes of the pressure distribution on the maximum area shown in Figures 6(a) and (c). The graphs in Figures 6(b) and (d) clearly illustrate that the pressure is low at the edge of the front mid-section surface of the nose-wheel fork, then increases to a maximum before starting to drop. It is also noted that the pressure is more evenly distributed on the surface of the optimised fork than on the original fork, as shown in Figure 6(d), leading to the adherence of airflow on the surface. This was not the case on the original fork because the pressure rapidly varied across its surface, allowing airflow recirculation. A notable difference in pressure distribution was observed at the front of the fork, where the pressure peaked. On the blunt front surface of the original fork, the pressure rose sharply from 340 Pa to a maximum of 480 Pa. In contrast, at the corresponding location on the optimised fork, the pressure increased more gradually from -100 Pa to a maximum of 485 Pa (see Figures 6(b) and (e)). These phenomena were attributed to the blunt and profiled geometry of the original and the optimised nose-wheel forks, respectively.

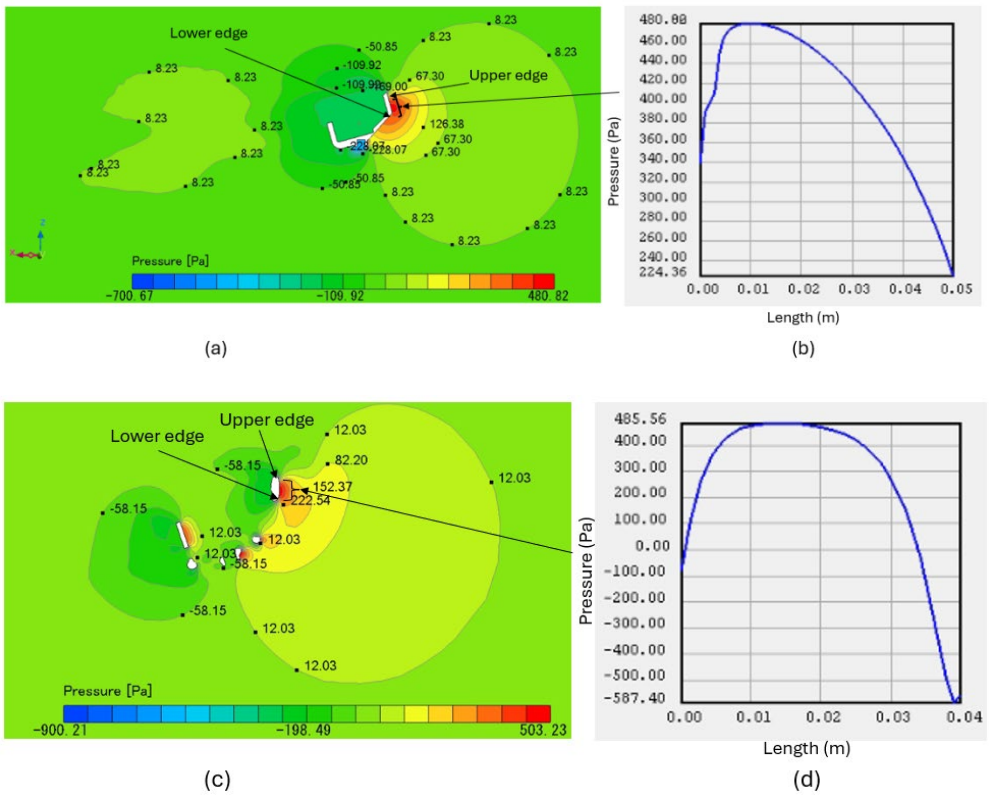

Figure 6: Detailed pressure distribution on the mid-section of the nose-wheel fork in plane ZX; (a) and (c) represent the pressure contour, whereas (b) and (d) show the graphs of the pressure recorded from the front surface of the original and optimised nose-wheel forks, respectively.

4.3. Wall shear stress

The surface streamline and wall shear stress (surface friction) generated on the original and the optimised nose-wheel forks are shown in Figure 7.

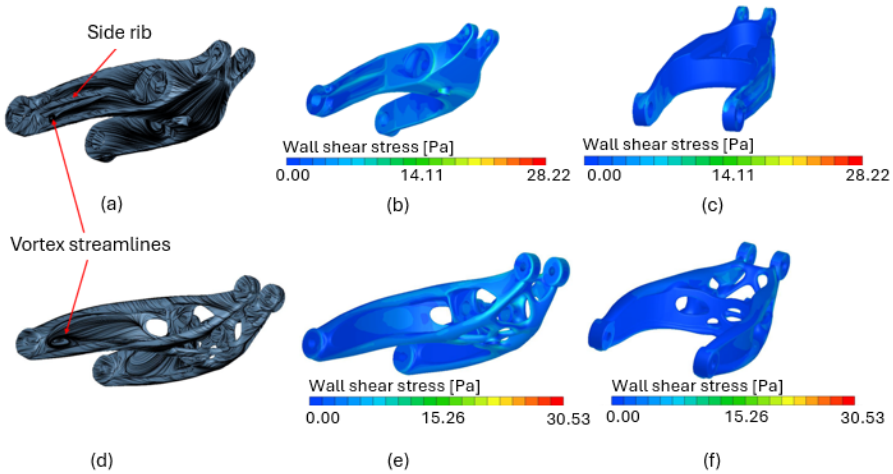

Figure 7: Illustration of the air streamlines and wall shear stresses (friction) in (a)-(c) for the original nose-wheel fork, and in (d)-(f) for the optimised fork.

The geometric differences between the original and optimised nose-wheel forks resulted in distinct surface streamlines around the fork, as shown in Figures 7(a) and (d). This is illustrated by the external side surface of the original fork experiencing double vortex streamlines between the side ribs, while the absence of a side rib on the optimised fork resulted in a single vortex air stream on the corresponding surface. Consequently, the original fork generated higher drag than the optimised fork because of the airflow separation caused by the formation of a double vortex. These different streamlines around the shape of the nose-wheel fork led to different shear stress and friction on the wall. In both the original and the optimised nose-wheel forks, very low wall shear stress was recorded, as shown in Figure 7.

4.4. Lift and drag forces

The drag, side, and lift forces experienced by the original and the optimised nose-wheel forks are given in Table 2. It should be noted that the total force in Table 2 comprises both pressure and shear stress components.

Table 2: Types of forces acting on the original and optimal nose-wheel fork

Fork condition	Parameters	Drag force (N)	Side force (N)	Lift force (N)
Original fork	Pressure	8.72	-2.52e-1	4.92
	Shear stress	0.48	1.03e-3	-4.10e-2
	Total	**9.20**	**-2.51e-1**	**4.88**
Optimised fork	Pressure	8.46	-5.78e-3	2.77
	Shear stress	0.59	-5.99e-5	-0.05
	Total	**8.97**	**-5.84e-3**	**2.71**

The magnitudes of the total drag forces are comparable between the original and the optimised nose-wheel forks. However, a significant difference in total lift forces was recorded when comparing the original and optimised forks. This was attributed to the 20% reduction in weight [24] and the organic shape of the nose-wheel fork that resulted from topology optimisation. In Figure 8, the drag and lift forces are graphically presented.

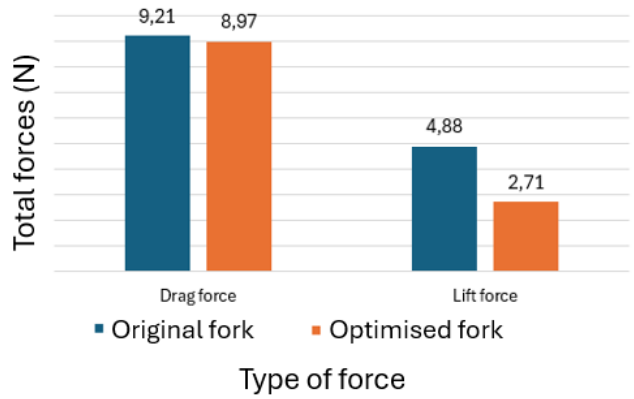

Figure 8: Graphical representation of the total drag and the lift forces of the original and topologically optimised nose-wheel fork.

The drag force of the optimised fork was 3% less than that of the original fork, whereas the lift forces on the optimal fork were found to be 44% more than those on the original fork. This implies that the topologically optimised nose-wheel fork would require less force to achieve similar lift to the original one. This behaviour is attributed to the lower weight and pressure difference across the surface of the optimised nose-wheel fork.

Topology optimisation of the AHRLAC nose-wheel fork was reached by inducing voids in the design domain following a mathematical algorithm with an objective to reach a balanced strength-to-weight ratio [31]. These voids provided airflow channels that increased the velocity and reduced the pressure on the upper surface of the optimised nose-wheel fork, while retaining higher pressure on the lower surface of the nose-wheel fork. This pressure difference promoted better lift on the topologically optimised nose-wheel fork than on the original one. Consequently, the optimised fork increased lift forces by 44% compared with the original nose-wheel fork. Moreover, the optimised geometry diminished the airflow recirculation around the surface of the fork, thus limiting the possibilities of airflow separation, which is known to increase drag [32]. To sum up: the resulting geometry from topology optimisation would improve the fuel efficiency of an aircraft by improving the lifting forces, reducing drag, and weight.

5. CONCLUSIONS

From the CFD studies of the original and the topologically optimised nose-wheel forks of the light aircraft, the following conclusions could be drawn:

- The airflow on the surface of the original nose-wheel fork generated recirculation owing to the absence of flow channels. This was not the case for the topologically optimised fork, since it provided smooth airflow through its voids.
- The topologically optimised nose-wheel fork had a higher pressure difference of 56.67% between the upper and lower surfaces, whereas the original fork had a lower pressure difference of 38.07%. Therefore, the topologically optimised nose-wheel fork improved the pressure difference by 18.6 % over the original fork. It could thus be concluded that the topologically optimised nose fork would promote lift better than the original fork. This would be enhanced by a 20% weight reduction obtained through topology optimisation.
- The different surface contours of the original and the optimised forks resulted in different streamlines and wall shear stress on the surfaces. The topologically optimised fork promoted lift by 44% and reduced drag by 3% compared with the original fork. Therefore, topology optimisation applied to structural aircraft components would not only improve the strength-to-weight ratio but would also have the potential to enhance the aerodynamic performance by reducing drag and improving lift.
- Future research should focus on validating the aerodynamic performance of the topologically optimised SLM Ti6Al4V(ELI) components using physical experimentation. This would demonstrate the accuracy of applying CFD to predict aircraft structural components, since the effect of surface roughness and thermal effects would also be incorporated.

ACKNOWLEDGEMENTS

The authors express their gratitude to the Central University of Technology, Free State, for providing the computer that was needed for this study. Hexagon through SIMTEQ Engineering is also acknowledged for the provision of the scFlow software applied during the CFD simulation. This research was funded by the South African Department of Science, Technology and Innovation through the Collaborative Programme in Additive Manufacturing [Contract No.: CSIR-NLC-CPAM-21-MOA-CUT-01 and CPAM-25-IND-03]. Financial support from the Chair in Innovation and Commercialisation of Additive Manufacturing is also gratefully acknowledged. Research and development support of the Central University of Technology, Free State, through the Emerging Researcher Programme of the capacity development grant, is also acknowledged.

REFERENCES

[1] **P.A. Kobryn, N.R. Ontko, L.P. Perkins, and J.S. Tiley**, "Additive manufacturing of aerospace alloys for aircraft structures," in *Proceedings of the RTO-MP-AVT-139 Cost Effective Manufacturing via Net-shape Processing*, Amsterdam, Netherlands, 2006.

[2] **A.M. Muiruri**, "Developing microstructure- and dislocation-based constitutive numerical models for predicting the mechanical behaviour of DMLS Ti6Al4V(ELI) at various strain rates." PhD thesis, Central University of Technology, Bloemfontein, Free State, 2021.

[3] **W.E. Frazier**, "Metal additive manufacturing: A review," *Journal of Materials Engineering and Performance*, vol. 23, no. 6, pp. 1917-1928, 2014. https://doi.10.1007/s11665-014-0958-z

[4] **R. Jones, R.K.S. Raman, A.P. Iliopoulos, J.G. Michopoulos, N. Phan, and D. Peng**, "Additively manufactured Ti-6Al-4V replacement parts for military aircraft," *International Journal of Fatigue*, vol. 124, pp. 227-235, 2019. https://doi.10.1016/j.ijfatigue.2019.02.041

[5] **A.A. Antonysamy**, "Microstructure, texture and mechanical property evolution during additive manufacturing of Ti6Al4V alloy for aerospace applications," PhD thesis, University of Manchester, United Kingdom, 2012.

[6] **M.S. Yasin, A. Soltani-Tehrani, S. Shao, M. Haghshenas, and N. Shamsaei**, "A comparative study on fatigue performance of various additively manufactured titanium alloys," *Procedia Structural Integrity*, vol. 38, pp. 519-525, 2021. https://doi.10.1016/j.prostr.2022.03.052

[7] **S.**T. Chai and W.H. Mason. "Landing gear integration in aircraft conceptual design." Multidisciplinary Analysis and Design Center for Advanced Vehicles. Virginia Polytechnic Institute and State University, 1997. https://ntrs.nasa.gov/api/citations/19970031272/downloads/19970031272.pdf

[8] **F. Götten, D. Finger, M. Havermann, C. Braun, F. Gomez, and C. Bil**, "On the flight performance impact of landing gear drag reduction methods for unmanned air vehicle," in *Proceedings of the Deutsche Gesellschaft für Luft- und Raumfahrt*, Lilienthal-Oberth, Friedrichshafen, Germany, 2018. https://doi.10.25967/480058

[9] **S. Hällgren, L. Pejryd, and J. Ekengren**, "(Re)design for additive manufacturing," *Procedia CIRP*, 50, pp. 246-251, 2016. https://doi.10.1016/j.procir.2016.04.150

[10] **J. Zhu, H. Zhou, C. Wang, L. Zhou, S. Yuan, and W. Zhang**, "A review of topology optimization for additive manufacturing: Status and challenges," *Chinese Journal of Aeronautics*, vol. 34, pp. 91-110, 2021. https://doi.10.1016/j.cja.2020.09.020

[11] **M.G. Fanni, M. Shabara, and M.N. Alkalla**, "A comparison between different topology optimization methods," *Mansoura Engineering Journal*, vol. 38, no. 4, 4, 2020. https://doi.org/10.21608/bfemu.2020.103788

[12] **P.W. Christensen and A. Klarbring**, *An introduction to structural optimization*. Springer, 2009.

[13] **P. Sforza**, *Commercial airplane design principles: Wing design*. Butterworth-Heinemann, 2014. https://doi.10.1016/B978-0-12-419953-8.00005-X

[14] **T.J. Mauery, A. Alonso Cary, V. Lee, R. Malecki, D. Mavriplis, G. Medic, J, Schaefer, and J. Slotnick**, *A guide for aircraft certification by analysis*. Hampton, VA: NASA Langley Research Centre, 2021.

[15] **P.R. Spalart and V. Venkatakrishnan**, "On the role and challenges of CFD in the aerospace industry," *The Aeronautical Journal*, vol. 120, no. 1223, pp. 209-232, 2016. https://doi:10.1017/aer.2015.10

[16] **X. Ge, O.V. Vasilyev, G. de Stefano, and M.Y. Hussaini**, "Wavelet-based adaptive unsteady Reynolds-averaged Navier-Stokes computations of wall-bounded internal and external compressible turbulent flows," *AIAA Journal*, 58, 1-21,2019. https://doi.org/10.2514/1.J058428

[17] **M. Breuer, D. Lakehal, and W. Rodi**, "Flow around a surface mounted cubical obstacle: Comparison of LES and RANS-results," in *Computation of three-dimensional complex flows*, in series *Notes on numerical fluid mechanics (NNFM)*, vol 49, M. Deville, S. Gavrilakis, and I.L. Ryhming, eds. Springer, pp. 22-30, 1996.

[18] **P. Spalart and K. Mejia**, "Analysis of experimental and numerical studies of the rudimentary landing gear," in 49th AIAA Aerospace Sciences Meeting including the New Horizon Forum and Aerospace Exposition, Orlando, Florida, 2011.

[19] **T. Imamura, T. Hirai, K. Amemiya, Y. Yokokawa, S. Enomoto, and K. Yamamoto**, "Aerodynamic and aeroacoustics simulations of a two-wheel landing gear," *Procedia Engineering*, vol. 6, pp. 293-302, 2009. https://doi.10.1016/j.proeng.2010.09.031

[20] **D.J. Munk, G.A. Vio, and J.E. Cooper**, "Topology optimisation of representative aircraft wing geometries with an experimental validation," in *Proceedings of the International Forum on Aeroelasticity Structural Dynamics*, IFASD, Como, Italy,1-14, 2017.

[21] **S.N.A. Yusof, Y. Asako, N.A.C. Sidik. S.B. Mohamed, W.M.A.A Japar**, "A short review on RANS turbulence models," *CFD Letters*, vol. 12, no. 11, pp. 83-96, 2020. https://doi.org/10.37934/cfdl.12.11.8396

[22] **Altair**, *Inspire SolidThinking*. Altair Engineering Inc, 2020. https://altair.com/inspire

[23] **Simteq Engineering**, *Topology optimisation using Patran*. 2025. https://simteq.co.za/blog/topology-optimization-using-patran/

[24] **L.F. Monaheng, W.B. du Preez, N. Kotze, and M. Vermeulen**, "Topology optimisation of an aircraft nose-wheel fork for production in Ti6Al4V by the Aeroswift high-speed laser powder bed fusion machine," in *Proceedings of the 14th World Conference in Titanium, MATEC Web of Conferences*, vol. 321, 03013, 2020. https://doi.org/10.1051/matecconf/202032103013

[25] **L.F. Monaheng, W.B. du Preez, and C. Polese**, "Failure analysis of a landing gear nose-wheel fork produced in Ti6Al4V(ELI) through selective laser melting," *Engineering Failure Analysis*, vol. 153, 107548, 2023. https://doi.10.1016/j.engfailanal.2023.107548

[26] **Hexagon**, *New generation CFD software with multiphysics and general-purpose capabilities*. Hexagon, 2025. https://simteq.co.za/products/cfd-scflow-scstream/

[27] **F.R. Menter**, "Two-equation eddy-viscosity turbulence models for engineering applications," *AIAA Journal*, vol. 32, 8, 1994. https://arc.aiaa.org/doi/10.2514/3.12149

[28] **S. Hiremath and A.S. Malipatil**, "CFD simulations of aircraft body with different angle of attack and velocity," *International Journal of Innovative Research in Science, Engineering and Technology*, vol. 3, pp. 16965-16972, 2014. https://doi.10.15680/ijirset.2014.0310077

[29] **T.K. Sengupta**, *Theoretical and computational aerodynamics: Drag reduction analysis and design of airfoils*. John Wiley & Sons, 2015.

[30] **J. Anderson**, *Fundamentals of aerodynamics*, 6th ed., McGraw Hill Education, 2017.

[31] **M. Langelaar**, "Topology optimization of 3D self-supporting structures for additive manufacturing," *Additive Manufacturing*, vol. 12, Part A, pp. 60-70, 2016. https://doi.10.1016/j.addma.2016.06.010

[32] **J. Lei, S. Zhao, and S. Wang**, "Numerical study of aerodynamic characteristics of FSW aircraft with different wing positions under supersonic condition," *Chinese Journal of Aeronautics*, vol. 29, no. 4, pp. 914-923, 2016. https://doi.10.1016/j.cja.2016.06.006